Li Promoting Long Afterglow Organic Light-Emitting Transistor for Memory Optocoupler Module

Yusheng Chen, Hanlin Wang, Hu Chen, Weimin Zhang, Michael Pätzel, Bin Han, Kexin Wang, Shunqi Xu, Verónica Montes Garcia, Iain Mcculloch, et al.

ADVANCED MATERIALS
www.advmat.de

Li Promoting Long Afterglow Organic Light-Emitting Transistor for Memory Optocoupler Module

*Yusheng Chen, Hanlin Wang, Hu Chen, Weimin Zhang, Michael Pätzel, Bin Han, Kexin Wang, Shunqi Xu, Verónica Montes-García, Iain McCulloch, Stefan Hecht, and Paolo Samorì**

The artificial brain is conceived as advanced intelligence technology, capable to emulate in-memory processes occurring in the human brain by integrating synaptic devices. Within this context, improving the functionality of synaptic transistors to increase information processing density in neuromorphic chips is a major challenge in this field. In this article, Li-ion migration promoting long afterglow organic light-emitting transistors, which display exceptional postsynaptic brightness of 7000 cd m^{-2} under low operational voltages of 10 V is presented. The postsynaptic current of 0.1 mA operating as a built-in threshold switch is implemented as a firing point in these devices. The setting-condition-triggered long afterglow is employed to drive the photoisomerization process of photochromic molecules that mimic neurotransmitter transfer in the human brain for realizing a key memory rule, that is, the transition from long-term memory to permanent memory. The combination of setting-condition-triggered long afterglow with photodiode amplifiers is also processed to emulate the human responding action after the setting-training process. Overall, the successful integration in neuromorphic computing comprising stimulus judgment, photon emission, transition, and encoding, to emulate the complicated decision tree of the human brain is demonstrated.

1. Introduction

Artificial intelligence (AI) technology is imposing a paradigm shift in our society in view of its potential to profoundly improve the quality of life on our planet. Von Neumann's computing architectures, which are at the basis of modern computers, are characterized by a physical separation between the units responsible for information processing and those for data storage, rendering interactive processing of big data in AI technology severely limited by the calculation speed and the high-power consumption.[1] Conversely, in-memory calculation systems have more recently emerged in view of their drastically enhanced computation performance which has been achieved by eliminating all slow data access steps, upon relying exclusively on data stored in random-access memory. Such a platform can be realized upon the integration of crossbar arrays of synaptic transistors, by mimicking

Y. Chen, B. Han, K. Wang, S. Xu, V. Montes-García, P. Samorì
Université de Strasbourg
CNRS
ISIS
8 allée Gaspard Monge, Strasbourg 67000, France
E-mail: samori@unistra.fr

H. Wang
Beijing National Laboratory for Molecular Sciences
Key Laboratory of Organic Solids
Institute of Chemistry Chinese Academy of Sciences
Beijing 100190, P. R. China

The ORCID identification number(s) for the author(s) of this article can be found under https://doi.org/10.1002/adma.202402515

DOI: 10.1002/adma.202402515

H. Chen
School of Physical Sciences
Great Bay University
Dongguan 523000, China

W. Zhang, I. McCulloch
Physical Sciences and Engineering Division
KAUST Solar Center (KSC)
King Abdullah University of Science and Technology (KAUST)
KSC
Thuwal 23955-6900, Saudi Arabia

M. Pätzel, S. Hecht
Department of Chemistry & Center for the Science of Materials Berlin
Humboldt-Universität zu Berlin
Brook-Taylor-Str. 2, 12489 Berlin, Germany

I. McCulloch
University of Oxford
Department of Chemistry
Oxford OX1 3TA, UK

S. Hecht
DWI – Leibniz Institute for Interactive Materials
Forckenbeckstr. 50, 52074 Aachen, Germany

biological nervous systems, as widely utilized for pattern recognition tasks such as MNIST handwritten digit recognition.[2] Although the functionalities of synaptic transistors have been improved significantly during the last few years via state-of-the-art semiconductor technology,[3] three major challenges still need to be addressed. i) The synaptic connection network in the human brain features a 3D configuration and displays high-density of neuron signal transmission and processing. These features cannot be sufficiently emulated by making use of the widely-adopted crossbar array architecture.[4] ii) Synaptic transistors have so far expressed two synaptic functions, namely spike time-dependent plasticity (STDP) and short-term memory (STM) to long-term memory (LTM) transition.[5] However, the transition from the LTM to the permanent memory (PM) still needs to be demonstrated. In-depth research on this topic revealed that in mammalian nervous systems, the duration of Ca^{2+}-dependent synaptic memory is on the timescale of hours in the neuron whereas more persistent or solidified memory requires the aid of protein synthesis.[6] The controlled synthesis of materials capable to store information in a non-volatile manner by exploiting postsynaptic current (PSC) represents a promising pathway to mimic this function. iii) The integrate-and-fire is a key function of spiking neurons, with a threshold defining if the neurons fire or not.[7] However, achieving this decision-making process (fire) in neuromorphic electronic circuits requires the integration of synaptic transistors and current comparators, leading the technical complexity.[8] A potential strategy to achieve the same complex function by mastering a simpler fabrication process, in a platform exhibiting low power consumption, could rely on the design of unprecedented synaptic devices comprising a built-in threshold switch.

Compared with electrical signals which are nowadays well-established for digital computations, multiple optical signals can simultaneously function in the absence of mutual interference to enable processing of complex information. Hence, optical signals combine specific advantages such as anti-jamming, lower power consumption, and large bandwidth, paving the way toward their successful exploitation in optocoupler, optical communication, and photonic integrated circuits.[9] Upon inserting a floating gate structure in a hybrid organic light-emitting transistors (OLETs) architecture, it was possible to combine long afterglow light emission with a synaptic function resulting in long afterglow OLETs (LAOLETs), which featured simultaneously multiple functions, that is, light generation characteristic of light-emitting diodes, the signal amplification of field-effect transistors, and the synaptic current modulation by charge storage units.[10] At the same time, optically switchable organic field-effect transistors (OSOFETs) are another type of multifunctional device that can realize multi-level non-volatile current modulation by blending semiconducting polymers with photochemically switchable molecules such as diarylethenes (DAEs)).[11] One can foresee the use of synaptic light emission to trigger the photo-isomerization of DAEs in electronic devices as a route to mimic the LTM-to-PM transition. However, the high operational voltage and faint brightness in afterglow emission of LAOLETs have represented major bottlenecks for their application in memory optocouplers.

Increasing the capacitance of the dielectric layer by replacing SiO_2 to high-k materials is a conventional method that is employed to solve the above problems. Both inorganic and organic high k materials, including zirconia (ZrOx), neodymium-doped aluminum oxide (Al_2O_3:Nd), cross-linked poly(vinyl alcohol) (C-PVA), poly(vinylidene fluoride-trifluoroethylene-chlorofloroethylene) (P(VDF-TrFE-CFE)), have been embedded into OLET for decreasing the operation voltage to the amplitude of ≈20 V.[12] Moreover, the implementation of Li-ion doping into the dielectric scaffold as an electrolyte has been exploited to mimic versatile synaptic functions, including STDP and paired-pulse facilitation (PPF).[13] Herein, we propose a Li-ion (Li^+) doped high k dielectric material such as Al_2O_3 as an electrochemically active layer to fabricate highly efficient and low operation voltage LAOLETs. Boosted by the $LiAlO_x$ ionic layer, the LAOLETs displayed excellent field-effect mobility and maximum brightness corresponding to 1.90 $cm^2\ V^{-1}\ s^{-1}$ and 4000 cd m^{-2} respectively, when powered by a bias voltage of 10 V. Strong post-synaptic brightness (PSB) surpassing 7000 cd m^{-2} was observed, upon applying $V_{DS} = 10$ V and 1.0 Hz at $V_{GS} = 10$ V. The device architecture and material layers of the memory optocoupler are portrayed in **Figure 1a**. The platform comprises a LAOLET as synaptic light emission input, an OSOFET as a non-volatile current storage element, and a photodiode amplifier (PDA) as responsive power output. As illustrated in Figure 1b, the faint presynaptic stimulus triggers a limited Li^+ migration thereby yielding PSC that powers light emission in the LAOLETs. Importantly, light emission is only observed when the PSC of the LAOLETs exceeds the decision-making point (DMP), being ≈0.1 mA. Therefore, a built-in threshold switch has been successfully integrated into hardware for higher-dimensional data processing. Furthermore, upon using PSC-driven long afterglow emission to photo-encode the OSOFET, photo-isomerization of DAEs could be realized for non-volatile memory, which emulates the biological LTM-to-PM transition via memory protein synthesis occurring in the synaptodendritic compartment (Figure 1c). Complicated decision-to-action processing has been encoded by integrating the OSOFETs with a PDA, where output voltage can be spiked by the setting-PSC triggered long afterglow.

2. Results and Discussion

2.1. Deposition of High k Electrolyte Layer

The morphology of the Cr gate electrode before and after thermal annealing at 360 °C for 2 h was assessed by atomic force microscopy, as displayed in Figure S1a,b (Supporting Information), respectively. The root mean square roughness (R_{RMS}) of the Cr gate slightly increased from 0.85 to 1.10 nm, indicating that the Cr material does not undergo severe deterioration upon heating. A thin film bilayer of high-k materials $LaAlO_x/LiAlO_x$ was deposited on the Cr gate via spin-coating, as a dielectric layer and electrolyte layer, respectively. This $LaAlO_x/LiAlO_x$ thin film exhibits an R_{RMS} of 0.86 nm, allowing the use of facile, continuous deposition of multilayers (Figure S1c, Supporting Information). Notably, the blending ratio of metal ions in the electrolyte thin film can be tuned by precursor solution mixing and further evaluated by X-ray photoelectron spectroscopy (Figure S2, Supporting Information). The chosen atom ratios of La: Al and Li: Al amount to 50:50 and 17:83, respectively.

To systematically explore the function of Li-doping, synaptic transistors based on different electrolyte layers, AlO_x, and

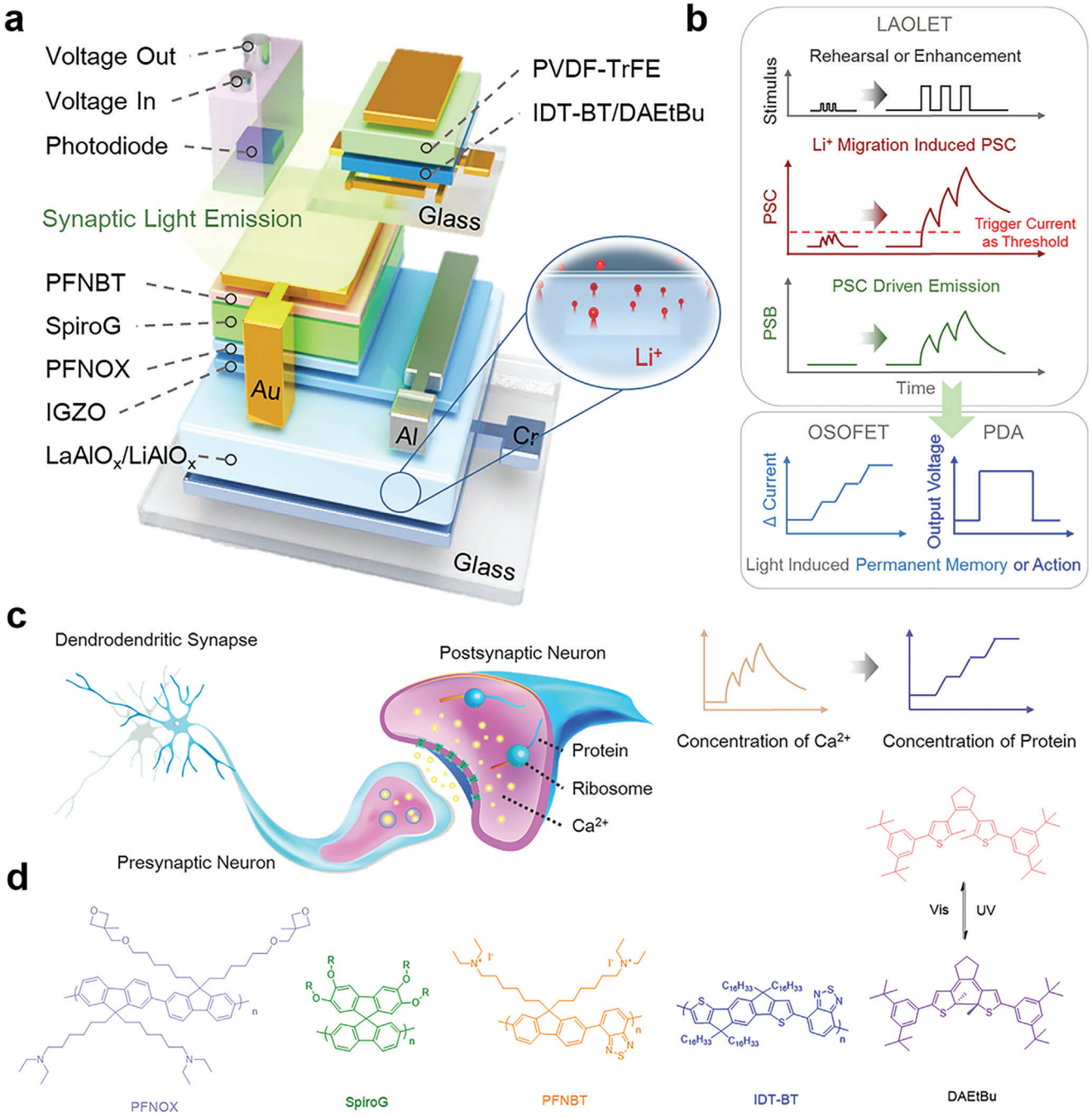

Figure 1. Setting-PSC triggered permanent memory record and action via memory coupler. a) Schematic diagram of memory optocoupler, where the bottom panel is LAOLET, the upper left panel is PDA and the upper right panel is OSOFET. b) Illustration diagram of the decision-making process of the memory coupler. c) Schematics of signal processing and storage in biological neurons. The long-term potentiation comprises an early and a late phase which are independent and dependent to the protein synthesis, respectively. The protein synthesized in the synaptodendritic compartment maintains a longer time than the Ca^{2+} permeated from the presynaptic neuron.[6b,14] d) Chemical structure of poly[9,9-bis(60-(*N*, *N*-diethylamino)hexyl)-fluorene-alt-9,9-bis(3-ethyl(oxetane-3-ethyoxy)-hexyl)-fluorene] (PFNOX), green light-emitting spiro-copolymer (SpiroG), poly(9,9-bis(6-trimethyl-ammoniumiodide)-hexylfluorene-2,7-diyl-alt-(benzo[2,1,3]thiadiazol-4,7-diyl)) (PFNBT), poly(indacenodithiophene-*co*-benzothiadiazole) (IDT-BT) and1,2-bis(5-(3,5-di-tert-butylphenyl)−2-methylthiophen-3-yl)cyclopent-1-ene (DAEtBu).

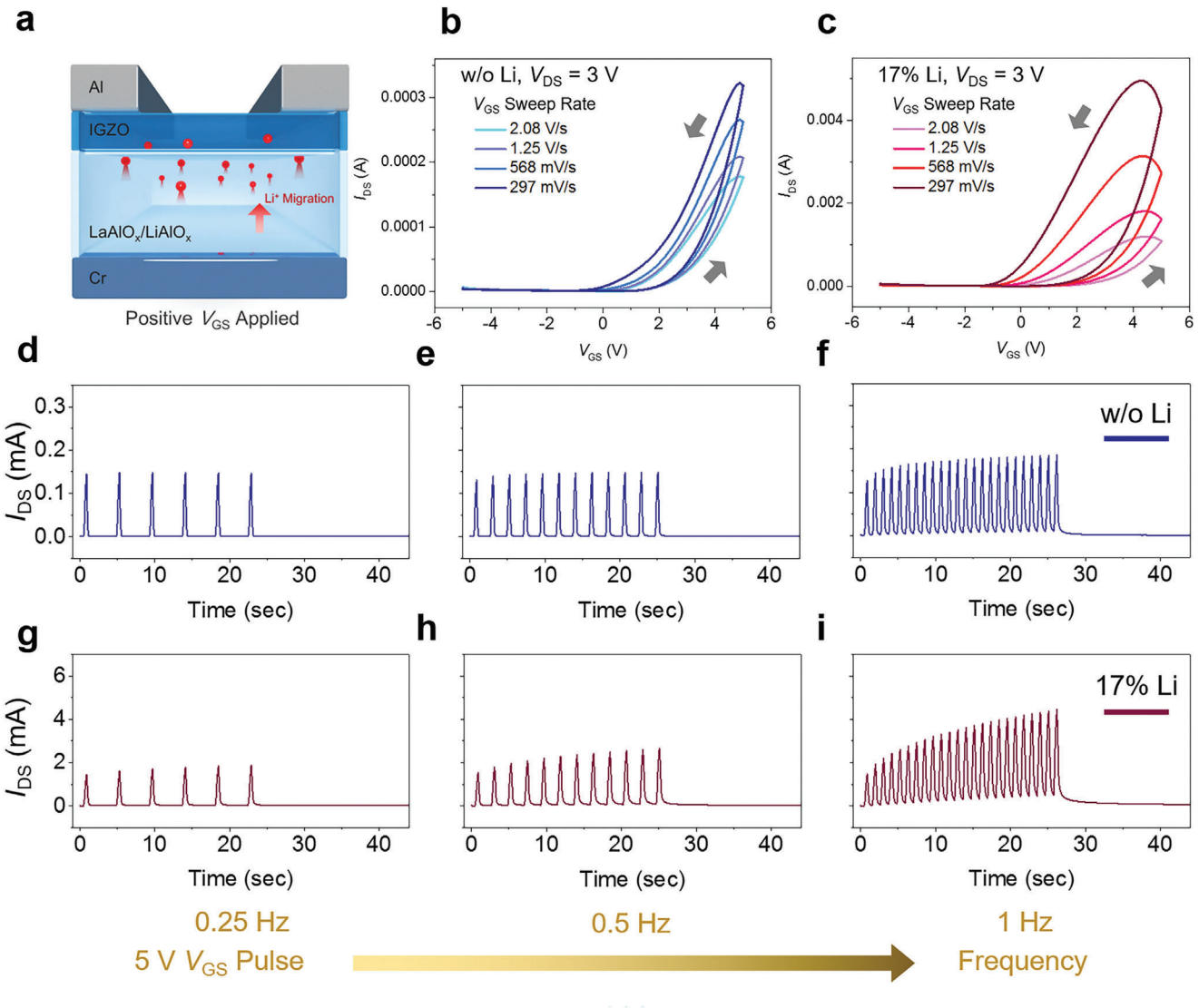

Figure 2. Reconfigurable synaptic behavior via Li^+ doping. a) Schematic diagram of synaptic transistor based on $LiAlO_x$ electrolyte, with the Li^+ migration supporting synaptic function. Transfer curves of synaptic transistors based on b) AlO_x and c) $LiAlO_x$, under various sweep ratios. Time-dependent measurement of AlO_x-based synaptic transistors carried out by positive V_{GS} spiked with the frequency of d) 0.25 Hz, e) 0.5 Hz, and f) 1.0 Hz, respectively. Time-dependent measurement of $LiAlO_x$-based synaptic transistors carried out by positive V_{GS} spiked with the frequency of g) 0.25 Hz, h) 0.5 Hz, and i) 1.0 Hz, respectively. The pulse width of V_{GS} spikes is set at 0.4 s.

$LiAlO_x$, were fabricated for comparison (**Figure** 2a). The transfer curves of these devices were measured under different sweep rates. As plotted in Figure 2b and Figure S3a (Supporting Information), AlO_x-based synaptic transistors exhibit lower mobilities of 1.60 $cm^2\ V^{-1}\ s^{-1}$, narrow memory window (qualified by shifted threshold voltage, ΔV_{Th}) of 1 V and scanned gate-source current (I_{GS}) hysteresis, which is ascribed to proton migration.[15] Upon doping the transistor with 17% Li^+ (Figure 2c), a tenfold enhancement in the field-effect mobility was observed, reaching 14.2 $cm^2\ V^{-1}\ s^{-1}$, larger anticlockwise drain-source current (I_{DS}) hysteresis of 3 V and I_{GS} hysteresis of 1 V, which can be interpreted by an increase of the moving ion concentration and Li^+ intercalation into the channel layer.[16]

The synaptic behavior of these transistors was explored by means of time-dependent characterizations, upon applying a V_{GS} of 5 V and V_{DS} of 3 V as presynaptic and postsynaptic inputs, respectively. Obviously, a stronger first PSC of $LiAlO_x$-based synaptic transistors was reached at 1.45 mA, which should be compared to the 0.14 mA first PSC of AlO_x-based synaptic transistors obtained when 0.25 Hz V_{GS} pulse applied (Figure 2d,g). Upon increasing the frequency of V_{GS} pulses, PPF in AlO_x-based synaptic transistors raises from 2.06% to 3.79%, 6.26%, 9.78%, and 13.1%, when 0.33, 0.5, 0.75, and 1.0 Hz V_{GS} pulses are spiked, respectively (Figure 2e,f; Figure S4a,b, Supporting Information). However, PPF in $LiAlO_x$-based synaptic transistors increases from 10.5% to 14.3%, 16.9%, 21.5%, and 28.5%, when 0.33, 0.5, 0.75, and 1.0 Hz V_{GS} pulses are spiked, respectively

(Figure 2h,i; Figure S4c,d, Supporting Information). The evolution of the PPF indexes of AlO_x-based, 8%-$LiAlO_x$-based, 17%-$LiAlO_x$-based synaptic transistors at different time intervals were plotted in Figure S5a (Supporting Information). We found an exponential decay with the increasing time interval of the V_{GS} pulse. The higher PPF values were observed in the devices with higher Li doping content, indicating the reconfigurable synaptic behavior originated from the Li^+ migration. The k value of $LaAlO_x/LiAlO_x$ was quantified by impedance measurements in a sandwiched capacitor of $Cr/LaAlO_x/LiAlO_x/Al$. From k-frequency (k--F) curves (Figure S5b, Supporting Information) the k value of $LaAlO_x/LiAlO_x$ was estimated as 12 at 1000 Hz, being drastically larger than the one of SiO_2 (3.9) which was used in previous studies.

2.2. Synaptic Light Emission in Low Voltage LAOLETs

Supported on the $LaAlO_x/LiAlO_x$ electrolyte layer, low voltage LAOLETs were fabricated by orthogonal spin-coating the indium-gallium-zinc oxide (IGZO), PFNOX, SpiroG, and PFNBT as channel layer, electron transport layer, light-emitting layer, and hole transport layer, respectively. The chemical structures of these compounds are reported in Figure 1d. The multilayered device architecture was visualized by cross-section scanning electron microscopy (SEM) imaging (**Figure** 3a). The performance of low-voltage LAOLETs was characterized subsequently.

The combined electrical/optical hysteresis transfer curves of low voltage LAOLETs were measured when a drain-source voltage (V_{DS}) of 10 V was applied and gate-source voltage (V_{GS}) was swept from −5 to 10 V and then back to −5 V (Figure 3b), revealing an anti-clockwise hysteresis of $\Delta V_{Th} = 5$ V. The operation mechanism of the LAOLETs is displayed in Figure 3c. When a positive gate voltage is applied, the mobile Li^+ ions in the electrolyte layer migrate toward the $LiAlO_x$/IGZO interface forming an electrical double layer (EDL),[17] and trigger the intercalation of some Li^+ ions into the IGZO channel yielding electrochemical doping which determine an increase of the free electron charges concentration in the channel.[16b,c,18] Both the EDL forming and electrochemical doping can enhance the conductance of IGZO. Once the gate voltage is removed, these displaced Li^+ ions are extracted for dynamic recombination, thus providing a sustainable enhancement of the mobility of the channel layer. During Li^+ migration, the electrons are injected from the source Al electrode into the electron transport layer through IGZO at a high conductivity state. At the same time, the hole carriers are injected from the drain Au electrode into the hole transport layer, leading to electron/hole recombination in the SpiroG emitting layer, thus yielding photon emission. This low-voltage LAOLET exhibits a superior field-effect mobility of 1.90 $cm^2\ V^{-1}\ s^{-1}$, an I_{ON}/I_{OFF} ratio of 10^3, and maximum brightness with green color emission of 4000 cd m^{-2}. Notably, these devices can be operated when higher both V_{DS} and V_{GS} of 12 V applied, yielding to mobility of 4.56 $cm^2\ V^{-1}\ s^{-1}$, a maximum brightness of 12 000 cd m^{-2}, and ΔV_{Th} of 8 V (Figure S6a, Supporting Information). More importantly, the trigger current of these devices was estimated being 0.1 mA. Herein, $I_{DS} = 0.1$ mA represents the DMP. In other words, when PSC is below 0.1 mA, no light emission is observed whereas when PSC exceeds 0.1 mA, light emission takes place as decision-making. The combined electrical/optical output curves of low voltage LAOLETs were also evaluated (Figure S6b, Supporting Information), which revealed a V_{DS} turning on the devices at ≈9 V. Optical images of devices under various V_{GS} were captured and displayed in Figure 3d.

To elucidate the synaptic behavior of LAOLETs, time-dependent measurements were carried out. First, a series of V_{GS} pulses of 2 V were applied as weak presynaptic stimulus and V_{DS} of 10 V was applied as postsynaptic terminals, as plotted in Figure 3e. Although PSC exhibits synaptic behavior with a PPF of 9.5%, the value of PSC after stimulus spiked is only ≈0.01 mA, being too low to power the light emission. Subsequently, different frequency V_{GS} pulses of 10 V were applied as a strong presynaptic stimulus. As plotted in Figure 3f–h, strong presynaptic pulses dramatically facilitate the PSC to 0.9, 1.3, and 3.0 mA in 24 s, when 0.25, 0.5, and 1.0 Hz V_{GS} is spiked. Under these conditions, the PSC is strong enough to drive the light emission of devices, resulting in postsynaptic brightness (PSB) as high as 3500, 4200, and 7000 cd m^{-2}. A higher frequency presynaptic input leads to a higher PSC and PSB, which represents the important synaptic behavior of STDP. Moreover, the PSC and PSB after 0.25 Hz and 0.5 Hz V_{GS} pulses decay rapidly, whereas an increased lifetime of PSC and PSB after 1 Hz V_{GS} pulses has been observed and it can be estimated from the fitting as 1.45 and 1.89 s (Figure S7a,b, Supporting Information), respectively. These results nicely demonstrate the STM-to-LTM transition as another important synaptic behavior.

2.3. Light Switchable Memory of Low Voltage OSOFETs

To demonstrate the LTM-to-PM transition, a low voltage OSOFET was fabricated on an ultra-flat glass substrate with transparency of 90% from 350 to 800 nm (Figure S8a, Supporting Information), in a top-gate bottom-contact configuration, with high k material, that is, poly(vinylidene fluoride-co-trifluoroethylene) (PVDF-TrFE, $k_{PVDF\text{-}TrFE} = 11.5$), employed as a dielectric layer (Figure S8b, Supporting Information). Photochromic molecules DAEtBu were blended with π-conjugated polymer IDT-BT in a 10% weight ratio, operating as a photo-switchable channel layer. DAEtBu exhibited excellent compatibility with IDT-BT, avoiding the occurrence of phase separation within the blend film (Figure S9, Supporting Information). The opto-electrical properties of OSOFETs based on the IDT-BT monocomponent films and their blends with DAEtBu were investigated. The chemical structures and energy levels of IDT-BT and DAEtBu are portrayed in Figure 1d and **Figure** 4a respectively. The photo-switchable current modulation of OSOFET is interpreted via the photo-isomerization process of DAEtBu. When DAEtBu undergoes photoswitching from the open-ring to the closed-ring isomer, its highest occupied molecular orbital level rises from −5.60 to −4.80 eV, yielding a trap for the hole carriers transported within IDT-BT, ultimately reducing the mobility of the device.

The transfer curves of IDT-BT-based devices are reported in Figure S10 (Supporting Information). They show that the control devices comprising IDT-BT neat films lacks a current photomodulation upon irradiation with UV light (λ = 312 nm, 0.3 mW cm^{-2}) and visible (Vis) light (λ = 530 nm, 10 mW cm^{-2}). In contrast, 10% DAEtBu blend transistors displayed a

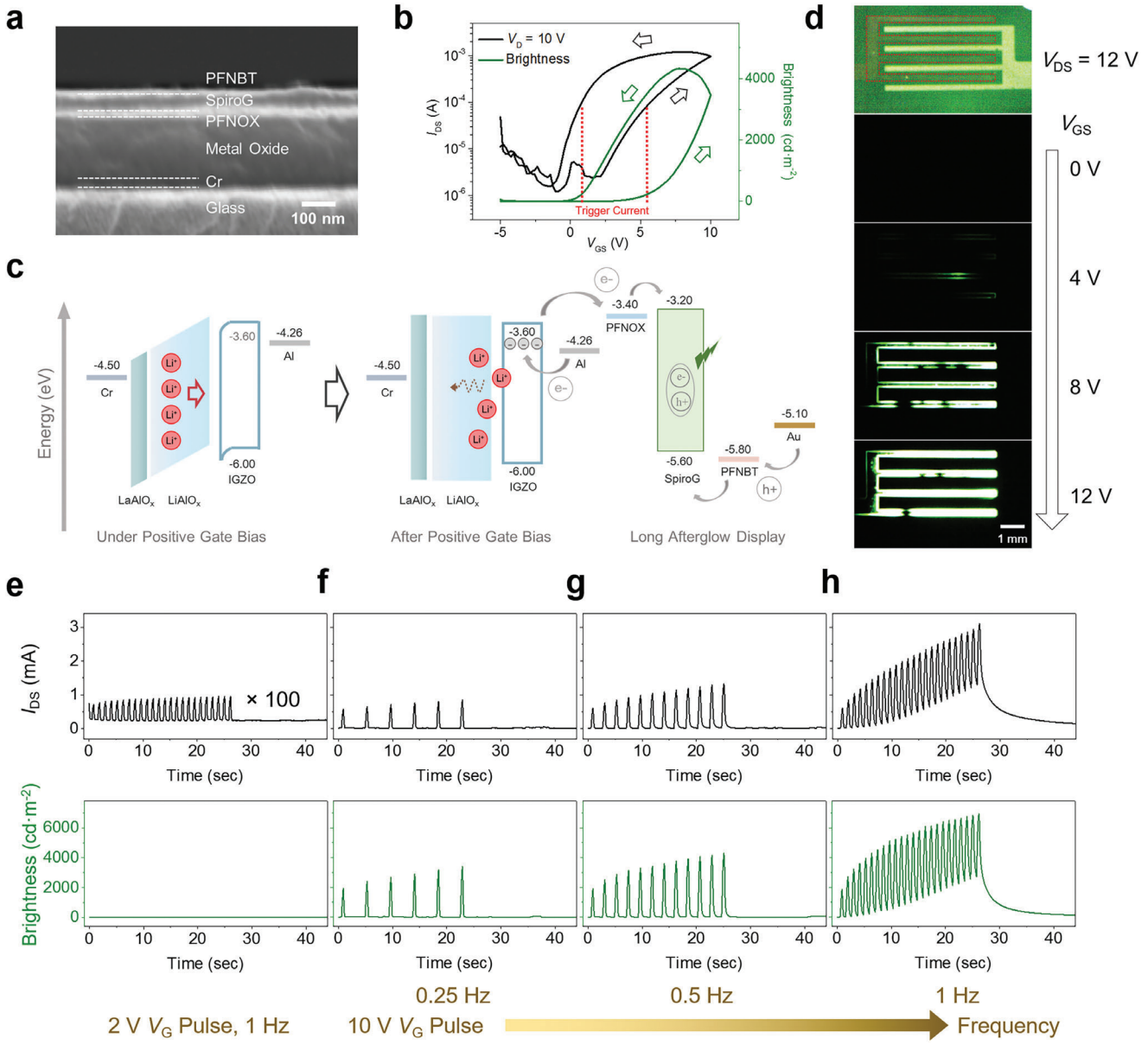

Figure 3. Electrical and optical characterization of low voltage LAOLETs. a) Cross-sectional SEM image of LAOLETs. b) Electrical and optical transfer curves of LAOLETs. The black and green lines represent the electric and brightness curves, respectively. c) Energy-level diagrams of LAOLETs representing the hole and electron recombination upon EDL formation. d) Optical images of LAOLETs when V_{DS} of 12 V and different V_{GS} are applied. e) Time-dependent measurement of LAOLETs carried out by weak positive V_{GS} spiked with the frequency of 1.0 Hz. Time-dependent measurement of LAOLETs carried out by positive V_{GS} spiked with the frequency of f) 0.25 Hz, g) 0.5 Hz, and h) 1.0 Hz, respectively.

well-defined photo-switching behavior. After the first 5 min UV light irradiation, I_{DS} of all devices decreased significantly, which is attributed to the generation energy trap states upon isomerization of DAEtBu ring-closure. Subsequent 10 min Vis light irradiation triggered the close-to-open back-isomerization thereby making it possible to restore the initial I_{DS}. The photo-modulation efficiency and photo-recovered efficiency of OSOFET in the second UV/Vis irradiation cycle were 98.2% and 99.6%, respectively. (Figure 4b).

For the sake of comparison, time-dependent investigations of OSOFETs with and without DAEtBu were carried out. To reset the measurement, the devices were initially irradiated with UV light for 5 min. Then, ten visible light pulses were applied as a switch-on stimulus (Figure S11, Supporting Information). Notably, a bias-stress effect has been observed in these devices because of the dipole polarization in PVDF-TrFE.[19] Because of this reason, the photocurrent was corrected by a bias-stress fitting line and then plotted in Figure 4c,d for analysis.[20] In the case of IDT-BT bare devices, each pulse of laser light irradiation determines a weak photocurrent of ≈0.06 μA. Such photoresponsive current originates from the photonic absorption of IDT-BT. In contrast, DAEtBu-blend devices present a higher photocurrent of ≈0.25 μA

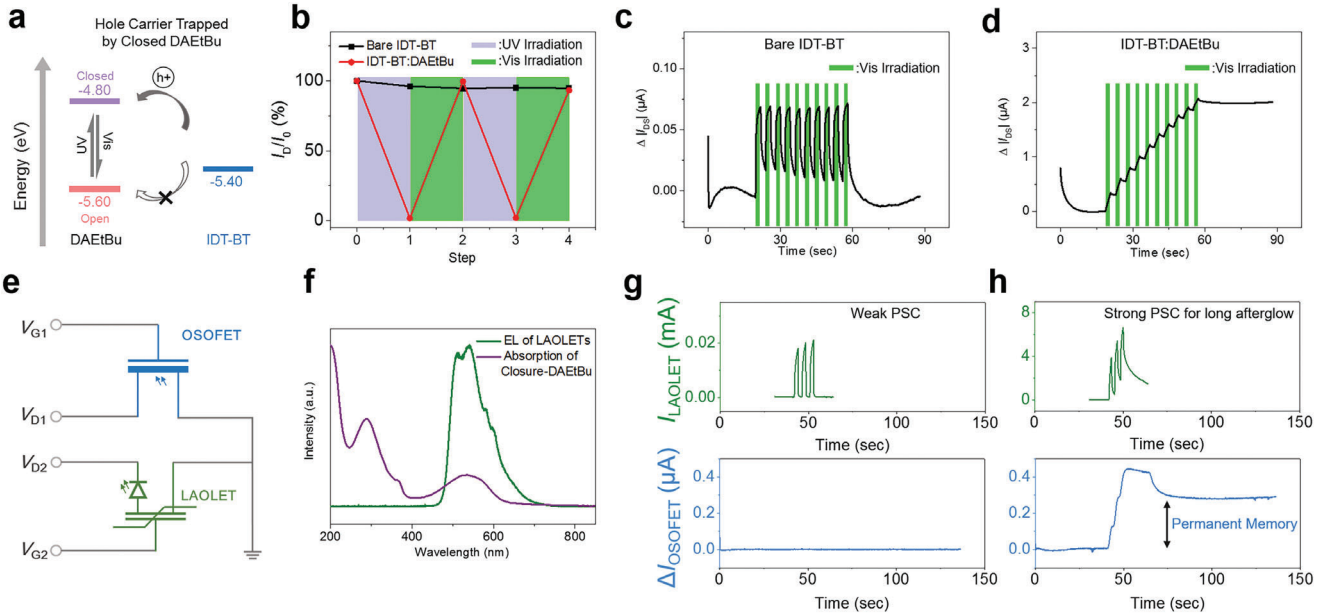

Figure 4. Characterization of OSOFETs and setting-PSC triggered neurotransmitter transfer memory optocoupler. a) Energy-level diagrams of OSOFETs representing the optically triggered charge trapping and untrapping process. b) Reversible I_{DS} modulation of IDT-BT/DAEtBu based OSOFETs upon cycling UV (312 nm, violet shaded areas) and Vis (530 nm, green shaded areas) light irradiation when V_{GS} of 10 V and V_{DS} of 8 V applied. I_{DS}–time changing curves (corrected for bias stress) in c) neat IDT-BT-based transistor and d) IDT-BT: DAEtBu transistor with irradiation of 530 nm laser for ten times through gate side. The width and interval of irradiation light are 2 and 3 s, respectively. e) Circuit diagram of PSC triggered neurotransmitter transfer memory optocoupler, including one LAOLET and one OSOFET, where V_{G1} = 10 V, V_{D1} = 8 V and V_{D2} = 12 V applied. f) Normalized spectra of electroluminescence (EL) of LAOLETs and absorption of close-state DAEtBu. Real-time measurement of memory optocoupler when three times of g) V_{G2} = 2 V and h) V_{G2} = 12 V applied, respectively.

as a result of Vis light irradiation. Furthermore, once the Vis light irradiation is removed, the photocurrent decays slightly and maintains a photo-memory current, underlining multi-levels photo-encoding capability. After ten pulses of Vis light irradiation, a photo-memory current of ≈2 μA was recorded (Figure 4d).

2.4. Realization of Memory Optocoupler

To implement the concept of neurotransmitter transfer in electronic devices via a light bridge, a pre-switch-off OSOFET was stacked onto the LAOLET. The circuit diagram of the setting-PSC triggered neurotransmitter transfer memory optocoupler is displayed in Figure 4e. Both normalized electroluminescence spectra of LAOLETs and absorption spectra of active materials in the OSOFET (ring-closure DAEtBu) were plotted in Figure 4f for comparison. The light emitted by the LAOLETs, spanning from 480 to 700 nm, can undoubtedly be absorbed by the DAEtBu's closed isomer, resulting in a synaptic light emission triggering the photo-isomerization process.

Real-time measurements of the memory optocoupler were carried out when the V_{G1} of 10 V, V_{D1} of 8 V, and V_{D2} of 12 V were applied. Initially, three pulses of V_{G2} of 2 V were performed as a weak presynaptic stimulus (Figure 4g; Figure S12a, Supporting Information). Drain-source current of LAOLET (I_{LAOLET}) was detected as PSC, increased from 0.018 to 0.022 mA. Obviously, this PSC is too weak to reach the DMP and it decays rapidly as volatile memory. Therefore, the recorded drain-source current of the OSOFET (I_{OSOFET}) record is negligible because of the absence of light irradiation. Different current outputs have been recorded when three enhanced V_{G2} of 12 V were applied (Figure 4h; Figure S12b, Supporting Information). Enlarged PSC at ≈mA amplitude was recorded, surpassing the DMP, indicating the successful activation of the long afterglow emission. Interestingly, a long-lasting photo-responsive current of 0.40 μA was recorded in the OSOFET from 40 to 65 s. Furthermore, after V_{G2} and V_{D2} removal at 65 s, the photomemory current of 0.30 μA was preserved, implying that the successful isomerization of the DAEtBu from the closed to the open state under the irradiation of PSB. In this way, the PSC spiked photic flux encodes a non-volatile current level, realizing the neurotransmitter transfer and LTM-to-PM transition.

To verify the performance of synaptic light as DMP in the logic decision tree, another memory optocoupler was investigated, whose equivalent circuit diagram is depicted in **Figure 5a**. Two pressure sensors (Sensor 1 in yellow and Sensor 2 in pink) were integrated with LAOLET and PDA to mimic the biological training and reaction terminal, respectively. As shown in Figure 5b, before training on Sensor 1, the pressure stimulus on Sensor 2 does not yield any response. In Figure 5c, a low V_{G3} of 2 V and three-times training pressure applied on Sensor 1 are operated in weak training processing of tactile information. In this case, the reaction terminal still does not respond to the pressure stimulus on Sensor 2, because the PSC of 0.02 mA does not achieve DMP. Intense training was realized by enhancing V_{G3} of 10 V and applying three-times of pressure on Sensor 1. As a result, the PSC of LAOLETs increased to 5 mA thereby triggering light emission. Furthermore, after this intense training, PSC maintains to power the long afterglow emission, which can spike the PDA for

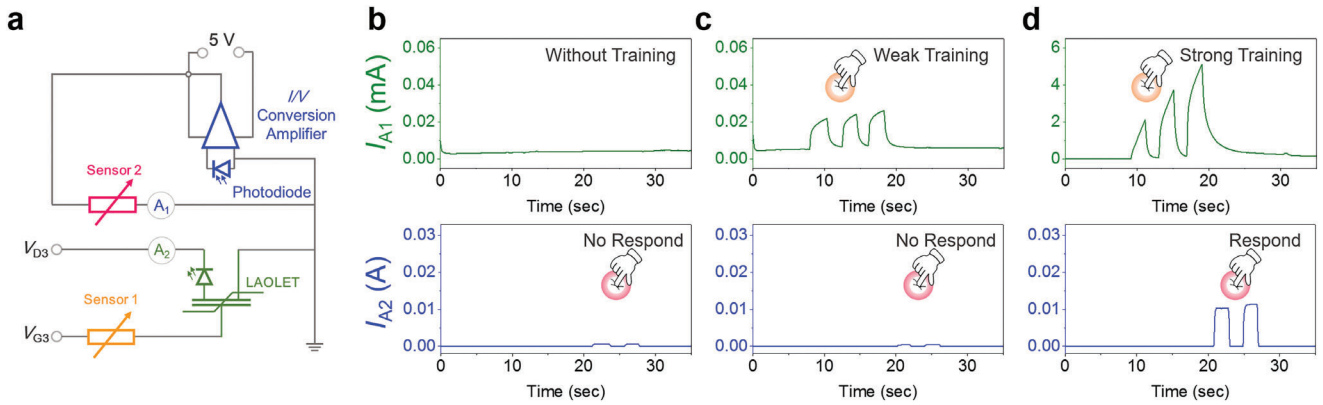

Figure 5. Characterization of setting-PSC triggered action memory optocoupler. a) Circuit diagram of PSC triggered action memory optocoupler, where $V_{G3} = V_{D3} = 10$ V applied. Real-time measurement of PSC triggered action optocoupler b) without training, c) with weak training, and d) with strong training, respectively.

converting the photocurrent to photovoltage output. During synaptic memory time, obviously current response to tactile on Sensor 2 was recorded (Figure 5d).

3. Conclusion

In summary, we have demonstrated that the reconfigurable synaptic behavior via Li^+ doping into electrolyte is a powerful approach to fabricate high-performance and low power-consumption LAOLETs endowed with a built-in threshold for firing decision (PSC = 0.1 mA). In particular, we showed that the long afterglow occurring in LAOLET can simultaneously realize the multifunctionality of in-memory calculation, light-emission, and decision-making process. Importantly, two memory optocoupler modules were achieved to prove the concept of synaptic electronic–photonic interaction in neuromorphic logic circuits. Upon integrating LAOLET and OSOFET, the PSC-driven PSB has been utilized to power photo-isomerization of DAEs, mimicking the LTM to PM transition in the human brain which can otherwise only be achieved via the cumbersome protein synthesis occurring in the synaptodendritic compartment. By combining LAOLET and PDA, the PSC-driven PSB has been utilized to mimic the decision-making process as an electrical voltage output.

In the future, memory optocouplers based on these multifunctional devices can emulate the artificial intelligent decision-tree (**Figure 6**). In an artificial brain, short-time stimulus or training spiked with a low PSC, that is, below DMP, yields a vanishing stimulus that corresponds to a volatile data storage. Conversely, rehearsal training can facilitate the PSC to exceed the DMP, thereby powering light emission for photo-encoding. The long afterglow can be capable not only to generate PM but also to turn on an output voltage for driving artificial versatile tissues, such as muscles.

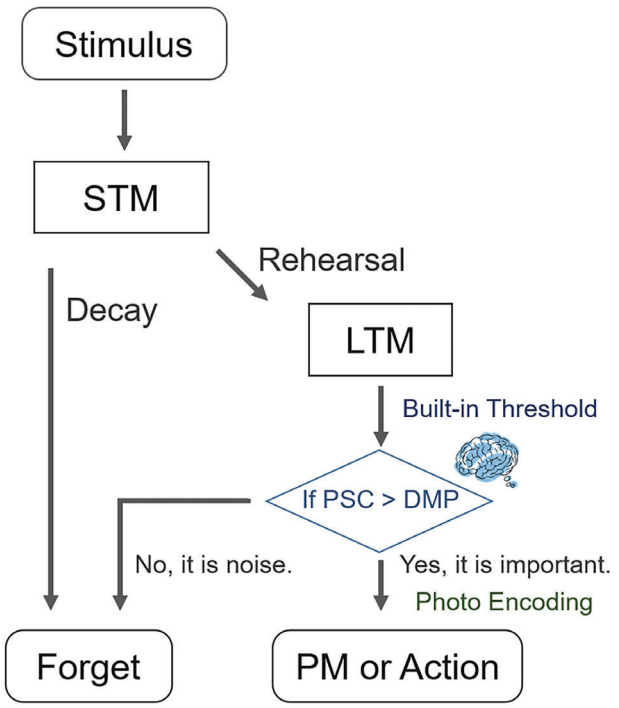

Figure 6. Decision tree of memory optocoupler based on multifunctional devices presented in this work.

Supporting Information

Supporting Information is available from the Wiley Online Library or from the author.

Acknowledgements

This work was financially supported by the Agence Nationale de la Recherche through the Interdisciplinary Thematic Institute SysChem via the IdEx Unistra (ANR-10-IDEX-0002) within the program Investissement d'Avenir, the Foundation Jean-Marie Lehn, the Institut Universitaire de France (IUF), the Chinese Scholarship Council, and the German Research Foundation (DFG via project 182087777–SFB 951). I.M. acknowledges financial support from KAUST Office of Sponsored Research CRG10, by EU Horizon 2020 grant agreement n°952911, BOOSTER, grant agreement n°862474, RoLAFLEX, and grant agreement n°101007084 CITYSOLAR, as well as EPSRC Projects EP/T026219/1, EP/W017091/1, and EP/L011972/1.

Conflict of Interest

The authors declare no conflict of interest.

Data Availability Statement

The data that support the findings of this study are available from the corresponding author upon reasonable request.

Keywords

electrolyte-based synaptic transistor, long-term memory to permanent memory transition, memory optocoupler modules, organic light-emitting transistors, synaptic light emission

Received: February 18, 2024
Revised: March 19, 2024
Published online:

[1] a) L. Shan, Q. Chen, R. Yu, C. Gao, L. Liu, T. Guo, H. Chen, *Nat. Commun.* **2023**, *14*, 2648; b) J. Lee, H. J. Bum, E. Kamaraj, D. Kim, H. Kim, S. Park, H. J. Park, *Nat. Commun.* **2023**, *14*, 5775; c) D. Kwon, S. Y. Woo, K. Lee, J. Hwang, H. Kim, S. Park, W. Shin, J. Bao, J. Kim, J. Lee, *Sci. Adv.* **2023**, *9*, eadg9123; d) H. Chen, Y. Cai, Y. Han, H. Huang, *Angew. Chem., Int. Ed.* **2024**, *63*, 2023136.

[2] a) J. Feldmann, N. Youngblood, M. Karpov, H. Gehring, X. Li, M. Stappers, M. Le Gallo, X. Fu, A. Lukashchuk, A. S. Raja, J. Liu, C. D. Wright, A. Sebastian, T. J. Kippenberg, W. H. P. Pernice, H. Bhaskaran, *Nature* **2021**, *589*, 52; b) X. Wang, C. Chen, L. Zhu, K. Shi, B. Peng, Y. Zhu, H. Mao, H. Long, S. Ke, C. Fu, Y. Zhu, C. Wan, Q. Wan, *Nat. Commun.* **2023**, *14*, 3444; c) K. Chen, H. Hu, I. Song, H. B. Gobeze, W. Lee, A. Abtahi, K. S. Schanze, J. Mei, *Nat. Photonics* **2023**, *17*, 629.

[3] a) H. Shim, F. Ershad, S. Patel, Y. Zhang, B. Wang, Z. Chen, T. J. Marks, A. Facchetti, C. Yu, *Nat. Electron.* **2022**, *5*, 660; b) T. Sarkar, K. Lieberth, A. Pavlou, T. Frank, V. Mailaender, I. McCulloch, P. W. M. Blom, F. Torricelli, P. Gkoupidenis, *Nat. Electron.* **2022**, *5*, 774; c) S. Wang, X. Chen, C. Zhao, Y. Kong, B. Lin, Y. Wu, Z. Bi, Z. Xuan, T. Li, Y. Li, W. Zhang, E. Ma, Z. Wang, W. Ma, *Nat. Electron.* **2023**, *6*, 281.

[4] a) D. Ham, H. Park, S. Hwang, K. Kim, *Nat. Electron.* **2021**, *4*, 635; b) Y. van de Burgt, A. Melianas, T. S. Keene, G. Malliaras, A. Salleo, *Nat. Electron.* **2018**, *1*, 386.

[5] a) Y. Chao, D. H. Ho, S. Kim, Y. J. Choi, I. C. Kwak, J. Min, H. Han, W. Gao, J. H. Cho, *Sci. Adv.* **2023**, *9*, eadg5946; b) A. Loeffler, A. Diaz-alvarez, R. Zhu, N. Ganesh, J. M. Shine, T. Nakayama, Z. Kuncic, *Sci. Adv.* **2023**, *9*, eadg3289.

[6] a) M. A. Sutton, E. M. Schuman, *Cell* **2006**, *127*, 49; b) C. R. Raymond, S. J. Redman, *J. Physiol.* **2006**, *570*, 97; c) W. C. Abraham, O. D. Jones, D. L. Glanzman, *npj Sci. Learn.* **2019**, *4*, 9; d) E. Pastalkova, P. Serrano, D. Pinkhasova, E. Wallace, A. A. Fenton, T. C. Sacktor, *Science* **2006**, *313*, 1141.

[7] a) Q. Xia, J. J. Yang, *Nat. Mater.* **2019**, *18*, 309; b) O. Krestinskaya, A. P. James, L. O. Chua, *IEEE Trans. Neural Netw. Learn. Syst.* **2020**, *31*, 4; c) D. S. Jeong, *J. Appl. Phys.* **2018**, *124*, 152002.

[8] a) F. Brückerhoff-Plückelmann, I. Bente, M. Becker, N. F. N. Vollmar, E. Lomonte, F. Lenzini, C. D. Wright, H. Bhaskaran, M. Salinga, B. Risse, W. H. P. Pernice, *Sci. Adv.* **2023**, *9*, eadi9127; b) H. Kweon, J. S. Kim, S. Kim, H. Kang, D. J. Kim, H. Choi, D. G. Roe, Y. J. Choi, S. G. Lee, J. H. Cho, D. H. Kim, *Sci. Adv.* **2023**, *9*, eadi3827; c) V. K. Sangwan, M. C. Hersam, *Nat. Nanotechnol.* **2020**, *15*, 517.

[9] a) B. Dong, S. Aggarwal, W. Zhou, U. E. Ali, N. Farmakidis, J. S. Lee, Y. He, X. Li, D. Kwong, C. D. Wright, W. H. P. Pernice, H. Bhaskaran, *Nat. Photonics* **2023**, *17*, 1080; b) L. Feng, M. Zhang, Z. Zhou, M. Li, X. Xiong, L. Yu, B. Shi, G. Guo, D. Dai, X. Ren, G. Guo, *Nat. Commun.* **2016**, *7*, 11985; c) Z. Li, R. Wang, G. Lihachev, J. Zhang, Z. Tan, M. Churaev, N. Kuznetsov, A. Siddharth, M. J. Bereyhi, J. Riemensberger, T. J. Kippenberg, *Nat. Commun.* **2023**, *14*, 4856; d) W. Bogaerts, D. Pérez, J. Capmany, D. A. B. Miller, J. Poon, D. Englund, F. Morichetti, A. Melloni, *Nature* **2020**, *586*, 207.

[10] a) Y. Chen, H. Wang, Y. Yao, Y. Wang, C. Ma, P. Samorì, *Adv. Mater.* **2021**, *33*, 2103369; b) Y. Chen, H. Wang, F. Luo, V. Montes-Garcia, Z. Liu, P. Samorì, *Sci. Adv.* **2022**, *8*, eabq4824.

[11] Y. Chen, H. Wang, H. Chen, W. Zhang, S. Xu, M. Pätzel, C. Ma, C. Wang, I. McCulloch, S. Hecht, P. Samorì, *Adv. Funct. Mater.* **2023**, *33*, 2305494.

[12] a) Z. Pan, K. Liu, Z. Miao, A. Guo, W. Wen, G. Liu, Y. Liu, W. Shi, J. Kuang, Y. Bian, M. Qin, M. Zhu, Z. Zhao, Y. Guo, H. Dong, Y. Liu, *Adv. Mater.* **2023**, *35*, 2209097. b) C. Zhao, H. Chen, M. U. Ali, C. Yan, Z. Liu, Y. He, H. Meng, *ACS Appl Mater Interfaces* **2022**, *14*, 36902; c) M. Xu, C. Zhao, Z. Meng, H. Yan, H. Chen, Z. Jiang, Z. Jiang, H. Chen, L. Meng, W. Hui, Z. Su, Y. Wang, Z. Wang, J. Wang, Y. Gao, Y. He, H. Meng, *Adv. Mater.* **2023**, *35*, 2307703; d) P. He, L. Lan, C. Deng, J. Wang, J. Peng, Y. Cao, *Mater. Horiz.* **2020**, *7*, 2439; e) H. Gao, Z. Miao, Z. Qin, J. Yang, T. Wang, C. Gao, H. Dong, W. Hu, *Adv. Mater.* **2021**, *33*, 2108795.

[13] a) Q. Liu, L. Yin, C. Zhao, Z. Wu, J. Wang, X. Yu, Z. Wang, W. Wei, Y. Liu, I. Z. Mitrovic, L. Yang, E. G. Lim, C. Z. Zhao, *Nano Energy* **2022**, *97*, 107171; b) R. D. Nikam, M. Kwak, J. Lee, K. G. Rajput, H. Hwang, *Adv. Electron. Mater.* **2020**, *6*, 1901100; c) R. Yu, Y. Yan, E. Li, X. Wu, X. Zhang, J. Chen, Y. Hu, H. Chen, T. Guo, *Mater. Horiz.* **2021**, *8*, 2797.

[14] J. Luboeinski, C. Tetzlaff, *Commun. Biol.* **2021**, *4*, 275.

[15] a) L. Zhu, C. Wan, L. Guo, Y. Shi, Q. Wan, *Nat. Commun.* **2014**, *5*, 3158; b) Y. He, L. Zhu, Y. Zhu, C. Chen, S. Jiang, R. Liu, Y. Shi, Q. Wan, *Adv. Intell. Syst.* **2021**, *3*, 2000210.

[16] a) J. Li, D. Jiang, Y. Yang, Y. Zhou, Q. Chen, J. Zhang, *Adv. Electron. Mater.* **2020**, *6*, 1901363; b) Y. Li, J. Lu, D. Shang, Q. Liu, S. Wu, Z. Wu, X. Zhang, J. Yang, Z. Wang, H. Lv, M. Liu, *Adv. Mater.* **2020**, *32*, 2003018; c) Q. Wang, T. Zhao, C. Zhao, W. Liu, L. Yang, Y. Liu, D. Sheng, R. Xu, Y. Ge, X. Tu, H. Gao, C. Zhao, *Adv. Electron. Mater.* **2022**, *8*, 2101260.

[17] H. Wang, Y. Chen, Z. Ni, P. Samorì, *Adv. Mater.* **2022**, *34*, 2205945.

[18] J. Rivnay, S. Inal, A. Salleo, R. M. Owens, M. Berggren, G. G. Malliaras, *Nat. Rev. Mater.* **2018**, *3*, 17086.

[19] a) N. V. Subbarao, M. Gedda, P. K. Iyer, D. K. Goswami, *ACS Appl. Mater. Interfaces* **2015**, *7*, 1915; b) S. Park, S. H. Kim, H. H. Choi, B. Kang, K. Cho, *Adv. Funct. Mater.* **2019**, *30*, 1904590.

[20] a) H. Qiu, Z. Liu, Y. Yao, M. Herder, S. Hecht, P. Samorì, *Adv. Mater.* **2020**, *32*, 1907903; b) T. Leydecker, M. Herder, E. Pavlica, G. Bratina, S. Hecht, E. Orgiu, P. Samorì, *Nat. Nanotechnol.* **2016**, *11*, 769.